Wiley
Structural Control and Health Monitoring
Volume 2024, Article ID 2326106, 20 pages
https://doi.org/10.1155/2024/2326106

WILEY

Research Article

Deformation Monitoring of High-Rise Building Clusters: Acquiring Deformation Coefficients by Combining Satellite Imagery and Persistent Scatterer Interferometry

Yun Zhou,[1] **Jianwei Chen**,[2] **Guanwang Hao**,[2] **and Shiqi Zhu**[2]

[1]*Key Laboratory for Damage Diagnosis of Engineering Structures of Hunan Province, Key Laboratory of Building Safety and Energy Efficiency of the Ministry of Education, College of Civil Engineering, Hunan University, Changsha, 410082, China*
[2]*College of Civil Engineering, Hunan University, Changsha, 410082, China*

Correspondence should be addressed to Jianwei Chen; cjw@hnu.edu.cn

Received 20 February 2024; Revised 2 June 2024; Accepted 13 June 2024

Academic Editor: Andrea Del Grosso

Persistent Scatterer Interferometry (PSI) is a remote sensing measurement technology based on electromagnetic waves, capable of simultaneously monitoring deformations in large urban building complexes with millimeter-level precision. However, relying solely on the line of sight (LOS) deformation sequence based on a specific permanent scatterer cannot accurately analyze building deformations, particularly in cases where high-rise buildings may simultaneously experience various deformation components such as temperature-induced deformation, shrinkage, creep, and tilting. To accurately identify the deformation states of high-rise buildings, the paper begins by systematically summarizing three typical deformation patterns from the unique perspective of synthetic aperture radar (SAR) satellites. These patterns include Pattern I, characterized by temperature-induced deformation alone, and Pattern II and Pattern III, which involve a combination of deformation in different directions relative to the SAR satellite in addition to temperature-induced deformation. To accurately monitor the LOS deformation of high-rise buildings, the paper introduces the concept of acquiring the evolutionary trends of temperature-related deformation coefficients and proposes a methodology for recognizing and quantifying deformation in high-rise buildings. Subsequently, this study utilized freely available Sentinel-1 satellite data to observe the deformation of nine high-rise buildings in Changsha, China. The research findings indicate that the thermal expansion coefficients of most high-rise buildings fall within the range of $6 \sim 12 \times 10^{-6}/°C$. High-rise buildings that have been constructed for more than ten years almost no longer experience significant shrinkage or creep, while new constructions may exhibit an initial shrinkage and creep of up to 1.2×10^{-4} mm/mm. Additionally, the study results demonstrate that super-tall buildings may exhibit centimeter-scale lateral deformations at their tops due to uneven shrinkage. Findings from the study indicate that the proposed method can achieve cost-effective and sustainable deformation monitoring of high-rise building clusters within a large urban area.

1. Introduction

The global trend of urbanization is expected to lead to a continual expansion of urban areas in the foreseeable future [1]. Concurrently, the rapid concentration of populations in urban areas unavoidably results in an increase in the number of buildings, posing a contradiction with the limited land area available. Consequently, many structures are compelled to achieve larger useable areas by adopting greater building heights. Meanwhile, the safety of high-rise buildings is consistently threatened due to factors such as the complexity of urban geological conditions [2], construction in close proximity to other structures [3], and the utilization of urban underground spaces [4]. An example is the tilting of the 184-meter Millennium Tower in California, USA, caused by changes in foundation conditions, resulting in horizontal displacements exceeding 40 cm at its top [5]. The changes in geological conditions also resulted in the collapse of the

Surfside Condominium in Miami, USA, in 2021 [6]. Therefore, it is essential to propose an efficient method for screening building risks to ensure the safety of urban high-rise building clusters during their service life. Given that the overall deformation pattern of a building directly reflects its overall stability, it is reasonable to deduce that accurately identifying the overall deformation pattern contributes to effective risk screening for high-rise buildings. However, the complex deformation components of high-rise structures, such as shrinkage [7] and temperature-induced deformations [8], pose challenges in accurately identifying the deformation pattern.

There are several commonly used methods for the deformation measurement of buildings, including geodetic measurements [9], sensor monitoring [10, 11], photogrammetric measurements [12, 13], laser scanning [14, 15], and ground-based radar observations [16, 17]. While these deformation measurement methods can achieve high precision, they are limited to monitoring deformations at specific points or within local areas of a structure. Therefore, when confronted with the practical demands of deformation monitoring for extensive high-rise urban structures, these commonly used methods for building deformation measurement will manifest significant shortcomings, such as limited field of view, high costs, and low efficiency. As a novel method for extensive deformation monitoring, space-borne synthetic aperture radar interferometry (InSAR) is expected to overcome the limitations of the abovementioned deformation measurement methods. The InSAR technique is a deformation measurement technology based on electromagnetic waves, utilizing the phase difference between SAR images recorded at different moments to compute the deformation of observed targets [18]. Multi-temporal InSAR (MT-InSAR) techniques, utilizing a series of SAR image sets, can now achieve deformation measurements of observed targets at a millimeter-scale precision [19]. Persistent Scatterer Interferometry (PSI) is a classic MT-InSAR technique proposed by Ferretti et al. [20]. PSI technology establishes a network by connecting all persistent scatterers (PSs) with strong and stable backscattering characteristics in the observed area, aiming to solve the line of sight (LOS) deformations of all PSs relative to a specific reference point [21]. PSs can often be identified along roadsides and buildings [22], providing favorable conditions for using PSI technology to monitor structural deformations. Regarding the accuracy of PSI, Ferretti et al. [23] demonstrated the submillimeter-level deformation monitoring accuracy of the PSI technology, utilizing a precision-moved artificial corner reflector. Karila et al. [24] and Yang et al. [25] used C-band and X-band satellite data, respectively, and compared the deformation results of PSs on individual buildings with precise leveling measurements, which confirmed the millimeter-level accuracy of PSI technology in practical building deformation monitoring.

Early studies on large-scale building clusters using PSI technology did not refine the research to the level of detailed deformation analysis at the individual building scale [26–28]. However, more recent studies have undertaken a detailed analysis of the deformation of individual buildings using the deformation-time series of PSs distributed on building rooftops. Bianchini et al. [29] utilized PSI technology to identify the uneven settlement of buildings, achieving results consistent with actual surveys. Liu et al. [4] and Drougkas et al. [30] utilized the deformation results from PSs on the top surface of the building to fit the inclined plane of the structure, thereby enhancing the accuracy of building risk assessment, although it did not consider the interaction between the structure and soil layers. To address the interaction between buildings and underlying soil layers, Macchiarulo et al. [31] proposed an improved method for building risk assessment by integrating ground settlement results identified through PSI technology with an equivalent beam model of the structure. Additionally, there are scholars who analyze the overall deformation of individual buildings by examining the deformation results of PSs on the building facade. Wu et al. [32] analyzed building deformations by examining the LOS deformation-time curve of a specific PS on the building façade, although the results of the analysis are prone to significant interference from temperature-induced deformations in tall buildings. Zhu et al. [33] utilized a composite function incorporating linear and sine functions to fit the seasonal deformation curve of PS on buildings, enabling the analysis of building deformation trends but introducing a complex iterative process. Gernhardt and Bamler [34] and Ma et al. [8] observed temperature-induced deformations in reinforced concrete high-rise buildings of a magnitude similar to the thermal expansion coefficient of steel and concrete material using high-resolution images from TerraSAR-X satellites. Subsequently, by excluding the temperature-induced deformation components of PSs, the millimeter-scale shrinkage, creep, and overall settlement of buildings can be discovered.

Due to the complexity of the upper surfaces of high-rise buildings, achieving a satisfactory density of PSs for the identification of building deformation patterns is full of challenges. The feasibility of utilizing PSs on building facades for refined monitoring of high-rise structures is more promising, but the existing research in this area is relatively limited. Moreover, current research relies on the utilization of expensive high-precision imagery data, such as from TerraSAR-X or COSMO-SkyMed, and involves intricate decomposition of the LOS deformation components of PSs. Additionally, existing studies have not systematically analyzed and summarized the deformation patterns of high-rise buildings from the unique observational perspective of SAR satellites.

Free access to Sentinel-1 satellite imagery data provided economical access to recognition of the deformations in high-rise buildings. Sentinel-1 is a C-band SAR satellite launched by the European Space Agency in 2013. It covers an area of 250 km in interferometric wide (IW) mode, with medium resolutions of 5 and 20 m in range and azimuth directions, respectively [35]. The objective of this study is to utilize freely available Sentinel-1 data with relatively lower resolution, omit the process of removing temperature-induced deformations, and propose an efficient deformation pattern recognition method for high-rise

buildings. The significance of the methodology proposed in this paper lies in its integration of architectural theoretical knowledge from civil engineering with PS-InSAR technology, enabling the development of an efficient and accurate method for identifying anomalous deformations in high-rise buildings, thus facilitating the widespread application of InSAR technology in urban building health monitoring.

The paper is organized as follows: Firstly, the background of the research and the current status of related studies are introduced. Secondly, the paper introduces the principles of PSI technology and proposes a method for the recognition of deformation patterns in high-rise buildings based on the temperature-related deformation coefficient. Thirdly, the temperature data and SAR image set required for the study are validated. Finally, the proposed method is used to recognize deformation patterns in nine high-rise buildings, followed by a comparative analysis.

2. Methodology

Figure 1 schematically illustrates the basic principles of InSAR technology for measuring architectural deformations. Initially, satellites pass over the construction area multiple times, emitting electromagnetic waves and recording the amplitude and phase information of the electromagnetic echoes in SAR images. Subsequently, the building's LOS deformation (denoted as D_{LOS}) can be calculated based on the interferometric phase between SAR images and the geometric relationship between the building and the satellite [36]. The space-borne SAR system provides a broad observational field for InSAR technology, and its susceptibility to weather conditions is minimal due to the characteristics of electromagnetic waves. These advantages provided the possibility of achieving a cost-effective, large-scale, and sustainable monitoring approach for high-rise buildings [37, 38].

2.1. PSI Technology. In this study, SAR image processing was conducted using the SARproz software, which has been validated for its reliability in previous research [39], with the main processing workflow illustrated in Figure 2. Initially, to mitigate decorrelation effects, a master image is selected based on the minimum temporal-spatial baseline principle, and the remaining slave images are registered to the master image, forming *N-1* interferometric pairs [39, 40]. Subsequently, the External Digital Elevation Model (DEM) is introduced for the interferometric processing of the images, and an appropriate amplitude stability index and temporal coherence threshold are determined for the identification of PSs. The PSs are then connected to form a Delaunay triangulation network, and the interferometric phase unwrapping is performed to obtain the actual phase differences between the PSs. Furthermore, atmospheric delay phases are estimated and removed to enhance the accuracy of deformation retrieval. Finally, the deformation sequences of PSs throughout the observation period are estimated using the interferometric phase calculation model, and these PSs will subsequently undergo geographic coding for visualization on Google Earth.

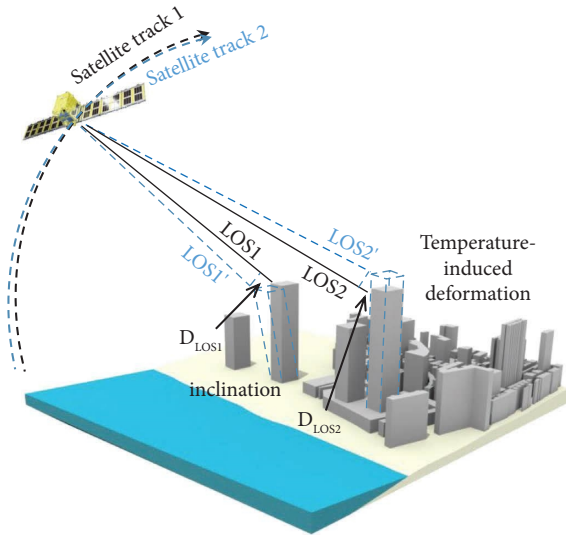

Figure 1: InSAR measurement principle diagram.

PSI technology accurately determines LOS deformations of observed targets by fitting the interferometric phase of PSs, employing a polynomial calculation model as illustrated in the following equation [41]:

$$\psi = \varphi_{\mathrm{ref}} + \varphi_{\mathrm{top}} + \varphi_{\mathrm{def}} + \varphi_{\mathrm{atm}} + \varphi_{\mathrm{noi}}, \tag{1}$$

where φ_{ref} represents the reference ellipsoid phase, φ_{top} is the terrain phase, φ_{def} is the deformation phase, φ_{atm} indicates the atmospheric delay phase, φ_{noi} represents the noise phase. The deformation phase can be obtained using the following equation derived from the above formula:

$$\varphi_{\mathrm{def}} = \frac{4\pi}{\lambda} t \cdot v + \frac{4\pi}{\lambda R sin\theta} B \cdot \varepsilon + \varphi_{\mathrm{res}}, \tag{2}$$

where λ represents the radar wavelength, R is the slant range from the radar to the ground target, and θ is the radar incidence angle; B denotes the spatial vertical baseline; ε represents DEM elevation error; t is the time baseline; v represents the linear deformation rate along the LOS direction; and φ_{res} is the residual phase of PSs, including nonlinear deformation, atmospheric phase, and noise.

The above equation can estimate the linear deformation rate of the observed target. However, it introduces significant bias when estimating the nonlinear deformations induced by temperature in high-rise buildings. Therefore, the following equation is used to improve the estimation of high-rise building deformation [42]:

$$\varphi_{\mathrm{def}} = \frac{4\pi}{\lambda} t \cdot v + \frac{4\pi}{\lambda R sin\theta} B \cdot \varepsilon + \frac{4\pi}{\lambda} T \cdot k + \varphi_{res}, \tag{3}$$

where T represents the temperature change between two images and k is the coefficient of thermal expansion. By performing second-order differencing on the connected PSs using the Delaunay triangulation network, the differential phase model can be obtained as follows:

$$\Delta\varphi_{\mathrm{def}} = \frac{4\pi}{\lambda} t \cdot \Delta v + \frac{4\pi}{\lambda R sin\theta} B \cdot \Delta\varepsilon + \frac{4\pi}{\lambda} T \cdot \Delta k + \Delta\varphi_{res}. \tag{4}$$

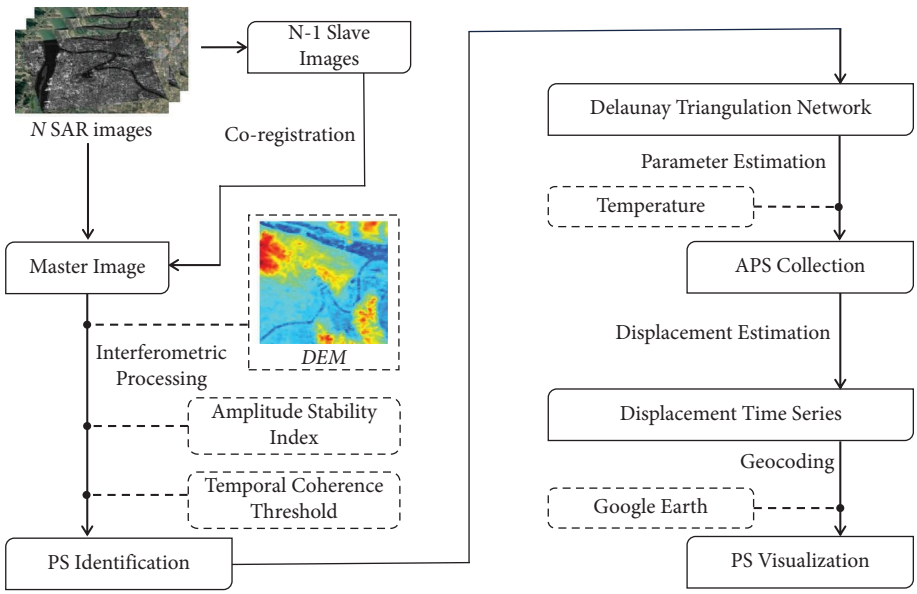

Figure 2: PSI workflow.

Using (5) transforms the problem of solving the deformation phase into an optimization parameter estimation problem that aims to maximize the coherence coefficient γ. In the equation, $\Delta\psi^i_{obs}$ is the observed phase difference, $\Delta\psi^i_m$ is the fitted value, and N is the number of PSs.

$$\gamma = \frac{1}{N}\sum_{i=1}^{N} \exp\left(j\Delta\psi^i_{obs} - \Delta\psi^i_m(\Delta v, \Delta\varepsilon, \Delta k)\right). \quad (5)$$

Based on the given reasonable range of linear deformation rates, building height, and accurate temperature information, by optimizing the three parameters Δv, $\Delta\varepsilon$, and Δk in (5), the LOS deformation of PSs can be obtained. Despite the evident temperature-induced deformation characteristics observed in the computed LOS deformation, it is noteworthy that such deformations are coupled with structural inclinations and other deformation components [8]. Therefore, this study categorizes such LOS deformation of tall buildings as temperature-related deformation and endeavors to propose an efficient method to overcome the interference caused by temperature-induced deformation, aiming to identify various deformation patterns of the high-rise building.

2.2. Deformation Patterns. When PSI technology is investigated for observing high-rise buildings, it is easy to identify PSs distributed along the height direction on the building facade. Since high-rise buildings are constructed on deep foundations, utilizing hard rock as a bearing layer, the building can be approximated as a vertical cantilever beam with the bottom end fixed to the ground, and the thermal expansion and contraction deformation of the building will be accumulated towards the top free end. Consequently, it can be found that on an annual time scale, these identified PSs often exhibit a sinusoidal temperature-related deformation pattern that is highly correlated with temperature and height. Therefore, to overcome the interference of fluctuating PS deformation-time curves in building deformation analysis, a thorough and systematic analysis of the deformation characteristics of high-rise buildings is essential.

2.2.1. Pattern I: Stable Temperature-Induced Deformation. To simplify the problem, the following assumptions were made before analyzing the deformation patterns of the high-rise building:

(1) It is assumed that only two PSs, namely PS_{top} and PS_{bot} (the subscripts "*top*" and "*bot*" respectively denote the top and bottom of the building), are located on a straight line on the building facade.

(2) It is assumed that the absolute values of temperature increase and decrease are equal, and that the temperature change is smooth. Additionally, it is assumed that the duration of temperature increase is equal to the duration of temperature decrease.

Figure 3(a) depicts the scenario where the building experiences only temperature-induced deformation. The structure undergoes expansion and contraction during time intervals of temperature increase and temperature decrease, respectively. In this paper, D^{top}_{LOS} and D^{bot}_{LOS}, respectively, denote the LOS deformations at the high and low points of the building. The LOS deformation is defined as negative values when moving away from the satellite. Figure 3(b) illustrates the stable deformation-time curve for the PSs, where t_i represents the moment of image acquisition, and T_i denotes the corresponding temperature at the moment of image acquisition. This paper defines such stable deformation as Pattern I, characterized by the stable nature of the enclosed area (A_i) between two PS deformation curves.

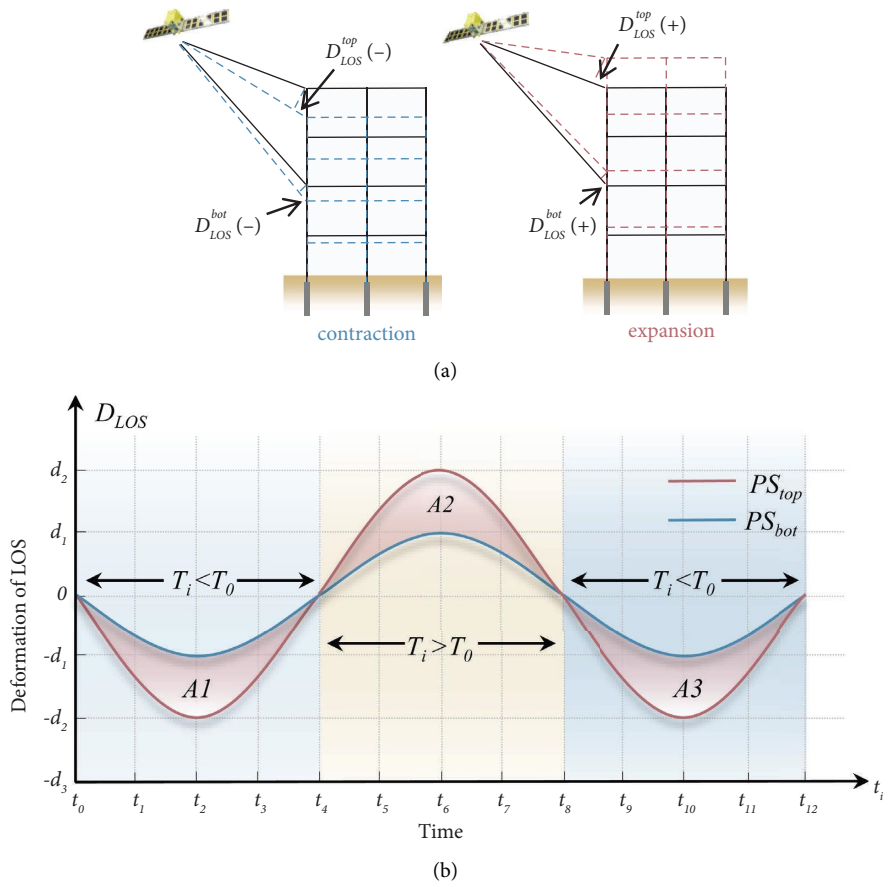

FIGURE 3: Deformation analysis of buildings under Pattern I. (a) Deformation characteristics of buildings. (b) LOS deformation characteristics of PSs.

2.2.2. Pattern II: Deformation Away from the Satellite. As depicted in Figure 4(a), the integration of Pattern I and deformations away from the satellite (involving building shrinkage, creep, and tilting) is termed Pattern II, resulting in a negative D_{LOS}. Due to the cumulative nature of the upward deformation in buildings, it will result in the absolute value of $D_{\mathrm{LOS}}^{\mathrm{top}}$ being greater than $D_{\mathrm{LOS}}^{\mathrm{bot}}$. Therefore, in the scenario of Pattern II, the negative trend in the deformation curve of the higher-positioned PS on the building is more pronounced. In Figure 4(b), it can be observed that area A_i exhibits the characteristics of $A_1 > A_2$ and $A_1 < A_3$. It is essential to indicate that the overall displacement of the building does not affect area A_i because it does not alter the relative deformations of the two PSs. Therefore, Pattern II can naturally exclude the component of overall building deformation caused by the slight instability of reference points in the PSs' deformation-solving process, such as resulting in the entire building deforming away from the satellite direction.

2.2.3. Pattern III: Deformation toward the Satellite. As shown in Figure 5(a), Pattern III deformation will emerge when the building experiences the deformation tilting toward the satellite in addition to the deformation associated with Pattern I. In this case, Figure 5(b) presents the opposite results compared with Figure 4(b), indicating $A_3 < A_1$ and $A_2 > A_1$. Like the analysis in Section 2.2.2, by quantifying the size of A_i, Pattern III can naturally exclude the component of overall building deformation that may arise from the instability of reference points in the PSs' deformation-solving process, causing the entire building to deform towards the satellite.

2.3. Temperature-Related Deformation Coefficient. As demonstrated in Section 2.2, based on various assumed conditions, accurately recognizing the magnitude of A_i enables the recognition of deformation patterns. However, in practical scenarios, the assumptions introduced in Section 2.2.1 are generally invalid. The nonfulfillment of assumption (1) has minimal impact because, in structural engineering, it is assumed that the distances between two points within the same plane of a building remain constant [43]. Thus, PSs at different positions within the same horizontal plane can equally represent the lateral deformation of the structure. However, the nonfulfillment of assumption (2) would pose computational challenges for A_i. Therefore, the concept of the temperature-related deformation coefficient was proposed to address the challenge of computing A_i and facilitate the recognition of deformation patterns in tall buildings.

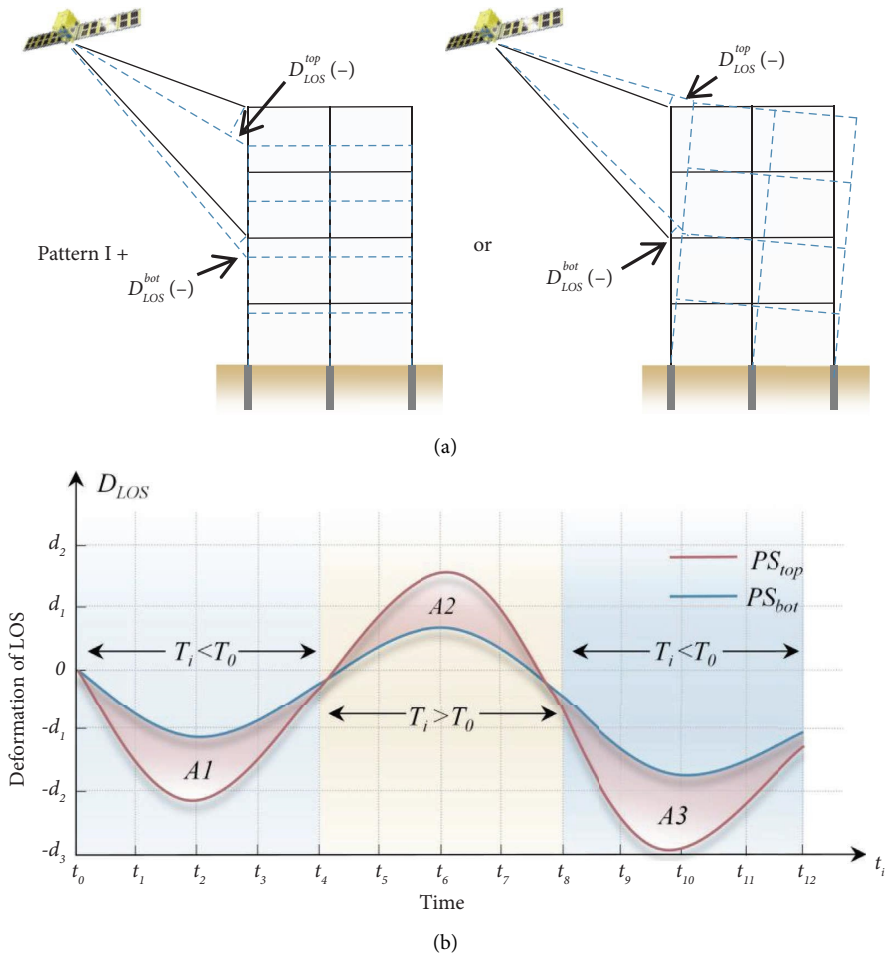

FIGURE 4: Deformation analysis of buildings under Pattern II. (a) Deformation characteristics of buildings. (b) LOS deformation characteristics of PSs.

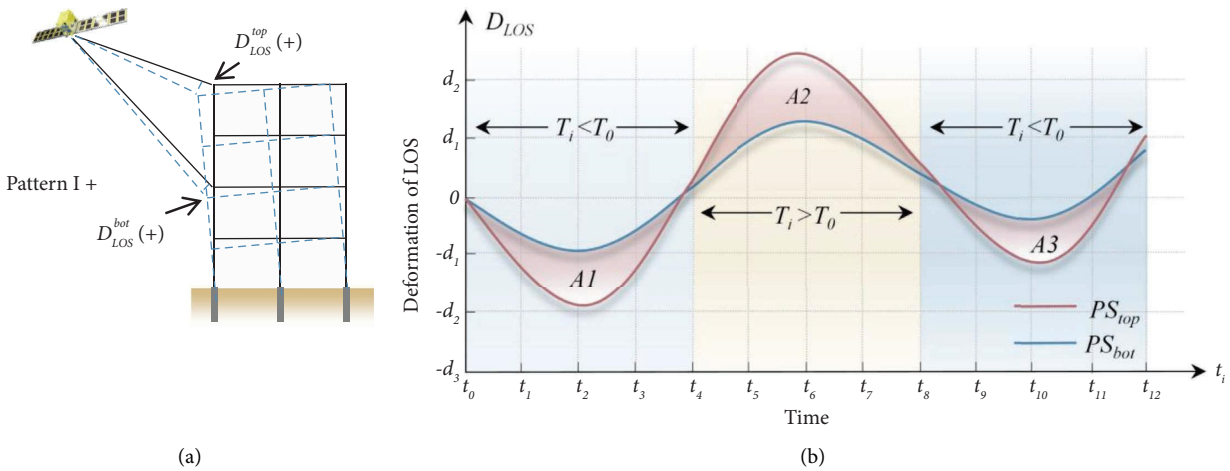

FIGURE 5: Deformation analysis of buildings under Pattern III. (a) Deformation characteristics of building. (b) LOS deformation characteristics of PSs.

Firstly, considering the scenario where only PS_{top} and PS_{bot} points exist on the building. Figure 6 illustrates the straightforward process for calculating temperature-related deformation coefficients. At each moment t_i if a slice can be taken, the D_{LOS} values of PS_{top} and PS_{bot} at that specific time can be extracted, denoted as D_{LOS}^{top} and D_{LOS}^{bot}. In the figure, T_0 and T_i represent the temperatures at t_0 and t_i, respectively, while H_{PS}^{top} and H_{PS}^{bot} represent the heights of the upper and

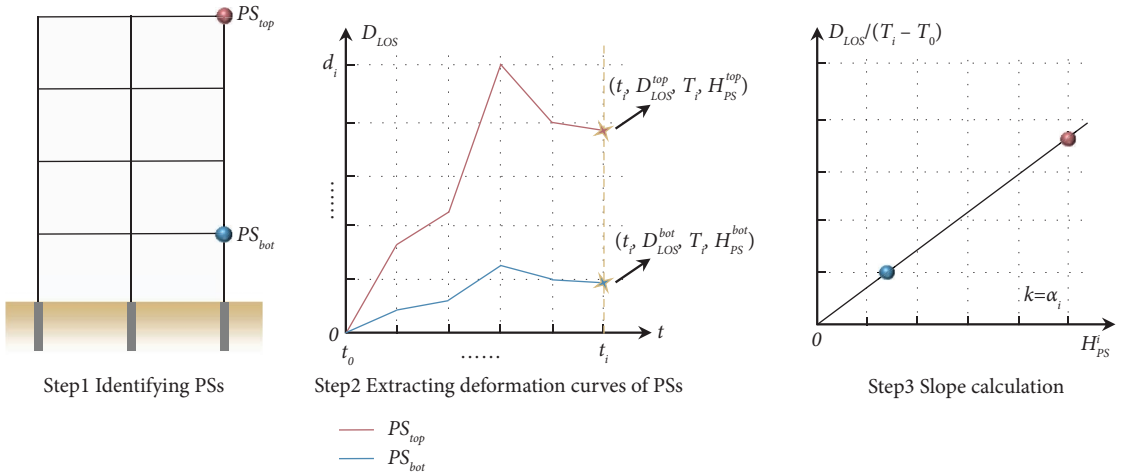

FIGURE 6: Simple calculation scenarios of temperature-related deformation coefficient.

lower PS points. Subsequently, the temperature-related deformation coefficient, namely α_i, can be defined by the following equation:

$$\alpha_i = \frac{D_{LOS}^{top} - D_{LOS}^{bot}}{(T_i - T_0)\left(H_{PS}^{top} - H_{PS}^{bot}\right)}. \tag{6}$$

It is noteworthy that α_i is comparable across different temperature conditions and various building heights, as the D_{LOS} is normalized in both temperature and height dimensions. However, in practice, solving α_i using only two PSs often yields highly discrete results due to the inherent noise or errors in LOS deformations estimated by PSI technology. In such situations, an improvement algorithm is proposed based on (6). Figure 7 illustrates the scenario where multiple PSs are present on the building facade, along with the approach for solving the coefficient α_i. In Figure 7, each PS is denoted as PS_i (where $i = 1, 2, \ldots, N$), the deformation of each PS is denoted as D_{LOS}^i (where $i = 1, 2, \ldots, N$), and the heights are represented as H_{PS}^i (where $i = 1, 2, \ldots, N$). It is noteworthy that the possible tilting deformation and temperature-induced deformation are linearly correlated with height. Similarly, shrinkage and creep also exhibit an approximately linear relationship with height [44]. Therefore, the temperature-related deformation coefficient α_i can be determined through a linear fitting method, as illustrated in Figure 7, and represented by the following equation:

$$D_{LOS}^i/(T_i - T_0) = \alpha_i H_{PS}^i + b_i. \tag{7}$$

For a specific PS, the value of $D_{LOS}^i/(T_i - T_0)$ is a constant, and the H_{PS}^i remains fixed. Therefore, (7) can be represented as

$$D^i = \alpha_i H_i + b_i, \tag{8}$$

where b_i is attributable to the overall offset error caused by PS localization and the variation in α_i. The objective of the linear fitting is to minimize the standard deviation in (9), resulting in the fitting results being highly sensitive to extreme outliers among certain PSs. Therefore, significant errors in the values of α_i will be easily identified and excluded from the analysis. Such significant errors might stem from inaccurate temperature inputs at certain instances or deformation noise caused by adverse weather conditions.

$$\sigma_i = \sqrt{\sum_{i=1}^{N} \frac{\left(D^i - f(H_i)\right)^2}{N}}. \tag{9}$$

2.4. Quantification Methodology for Building Deformation. In-depth analysis of building deformations requires not only a qualitative examination of the deformation patterns but also the quantitative identification of the magnitudes of deformation. In the following, a method for quantifying building deformations using the coefficient α_i is proposed.

Through the optimized solution of α_i, when the building deformation follows Pattern I or experiences overall settlement and uplift, α_i will remain stable. In this study, α_i is considered as stable status when the absolute deviation ($|\Delta\alpha|$) between α_i and its mean value is generally less than 1.0×10^{-6}/°C. This level of stability is deemed acceptable, as it is smaller than the building material's thermal expansion coefficient. The value of $|\Delta\alpha|$ can be calculated using the following equation:

$$|\Delta\alpha| = \left|\alpha_i - \sum_{i=1}^{N} \alpha_i/N\right|. \tag{10}$$

When the building undergoes Pattern II deformation, α_i will continuously increase within the cooling period and decrease within the warming period. In the case of Pattern III, the variation trend of α_i is reversed. In these two scenarios, the variation rate k of α_i can first be determined through linear fitting. Subsequently, for a building with a height H, the LOS deformation at the top (D_{LOS}^{top}) over a time span (Δt) can be calculated as follows:

$$\left|k \cdot \Delta t \cdot H \cdot (T_1 - T_0)\right| = \left|D_{LOS}^{top}\right|. \tag{11}$$

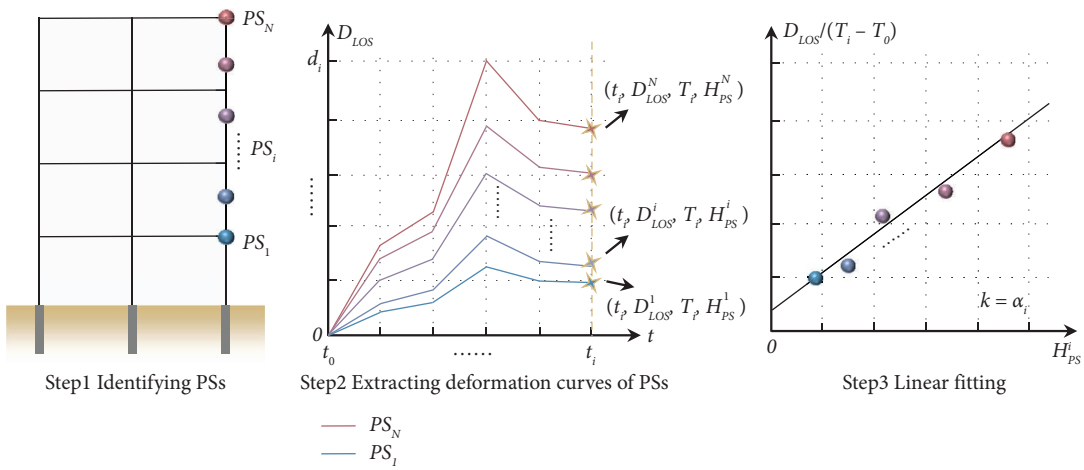

Figure 7: Improved algorithm for temperature-related deformation coefficient.

It is noteworthy that since the value of α_i for the first image corresponds to zero, the variable Δt represents the time span relative to the time of acquiring the second image. T_1 and T_0, respectively, denote the temperature values at the time of acquiring the second and first images.

3. Method Validation

3.1. Validation of the Temperature Data Acquisition Method. The deformation of high-rise structures is primarily induced by temperature variations. Therefore, reliable temperature data are crucial for the phase estimation in (4), directly impacting the accuracy of deformation solutions for PSs. The temperature around the building can be obtained through the European Center for Medium-Range Weather Forecasts (ECMWF) or from the meteorological stations at nearby airports. This study compares ECMWF temperature data with the actual values obtained from stain (temperature) transducers, thereby selecting the temperature dataset most suitable for high-rise building deformation solutions.

The transducers are installed on Shengtong Tower in Changsha City, China, which features a frame shear wall structure comprising Tower A, with a height of 279.65 meters across 59 floors, and Tower B, with a height of 219.65 meters across 49 floors. The average temperatures obtained on the 4th, 10th, 25th, and 31st floors of Tower A are considered the actual values for temperature in this study. The airport temperatures were sourced from Huanghua International Airport, and the ECMWF data were selected by directly pinpointing the location of Shengtong Tower. The relative positions of the mentioned locations and the installation positions of transducers can be found in Figure 8. More detailed information about the transducer instrumentation and the construction process of Shengtong Tower can be found in Zhou et al. [44]. The selected time for temperature comparison is 6: 00 PM in the GMT+8 time zone, corresponding to the imaging time of the Sentinel-1 satellite over Changsha City region. As this study was conducted during the construction phase of Tower A, it was only possible to retrieve complete temperature data from the sensors for the period of January to June 2023. As shown in Figure 9(a), both ECMWF and Huanghua International Airport temperatures exhibit high consistency with the sensor-recorded temperatures in terms of trends. Figure 9(b) illustrates the normal distribution of deviations present in the data from both Huanghua International Airport and ECMWF, indicating that the data from ECMWF exhibit more minor deviations. Therefore, this study selects temperature data from ECMWF for the following PSI deformation analysis.

3.2. Validation of the Sentinel-1 Dataset and PSI Technique. Kunlun Tower is a high-rise building with an approximate height of 100 meters. In 2013, a deep excavation operation conducted adjacent to Kunlun Tower posed a threat to its stability. To monitor the safety status of the building in realtime, Bao et al. [3] installed a GPS monitoring station on the top of Kunlun Tower, obtaining the building's east-west, north-south, and vertical displacement components during the period 2014 to 2016. To compare with the deformation obtained from GPS, this study selected a dataset of Sentinel-1 images and applied PSI techniques to calculate the deformation of the Kunlun Tower during the same period. Since the descending orbit view of the Sentinel-1 satellite can avoid the impact of construction on the west side of the Kunlun Tower on the coherence of the interferometric images, and a higher-confidence PS was identified at the top of the building, this study used the descending orbit image set for the validation process. Detailed information about the datasets of Sentinel-1 satellite imagery data are presented in Table 1, where B represents spatial baselines, t represents temporal baselines, and T represents the atmospheric temperature at the time of image acquisition from ECMWF. All images belong to descending data with an incidence angle θ of 32.29° and an azimuth angle α of 10.01°. The master image was acquired on March 2, 2015, and all the images were acquired at 6: 20 AM in the GMT+8 time zone.

As illustrated in Figure 10(a), utilizing the PSI technique outlined in Section 2.1, a PS was identified at the GPS station location, and the LOS deformation at the top of the building

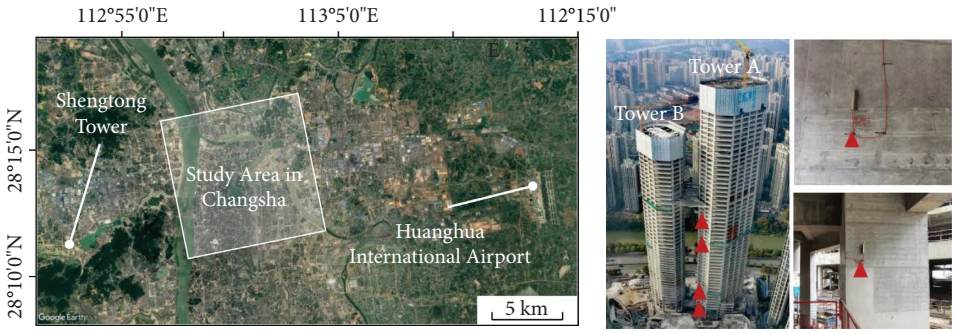

Figure 8: Aerial view of the Changsha city and the position of stain (temperature) transducers.

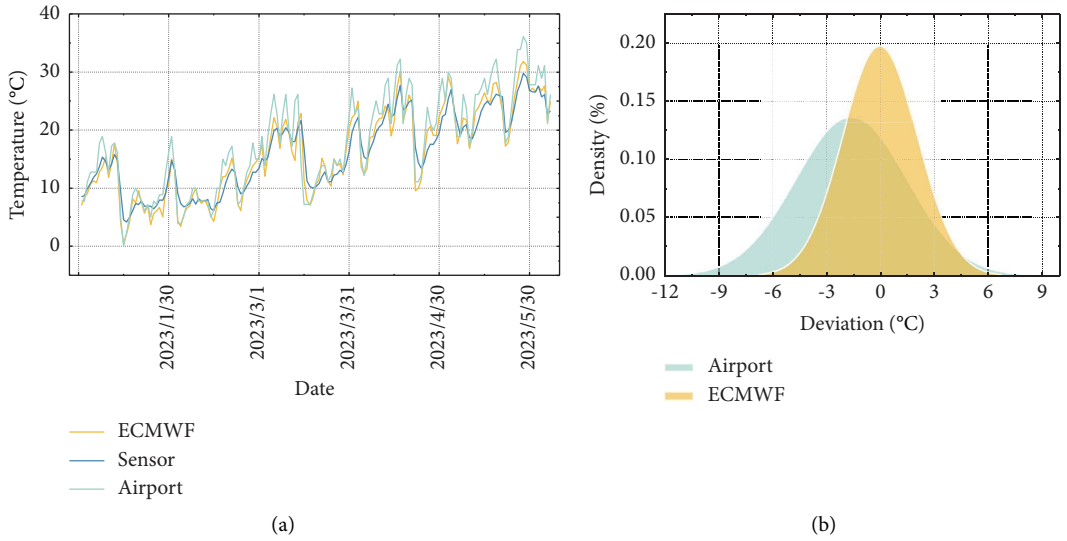

Figure 9: Temperature validation. (a) Temperature comparison. (b) Deviation statistics.

Table 1: Beijing SAR image dataset.

No.	Slave	B (m)	t (day)	T (°C)
1	2014/10/09	22.58	144	12.82
2	2014/11/14	131.70	108	−2.39
3	2014/12/08	−65.47	−84	−5.61
4	2014/01/01	−4.38	−60	−7.73
5	2015/01/25	−54.42	−36	−1.66
6	2015/03/26	154.80	24	7.17
7	2015/05/25	27.95	84	24.44
8	2015/06/18	−11.88	108	27.38
9	2015/07/24	11.95	−144	25.55
10	2015/09/10	21.54	192	19.24
11	2015/10/04	42.90	216	13.48
12	2015/11/09	46.64	252	1.57
13	2015/11/21	25.92	264	0.06
14	2015/12/15	−57.76	288	−0.65
15	2016/01/20	18.89	314	−7.59
16	2016/02/13	38.24	348	0.97
17	2016/02/25	−19.47	360	−2.94
18	2016/03/08	−44.53	372	−1.90
19	2016/03/20	−8.83	384	4.78
20	2016/04/13	66.89	408	11.57
21	2016/05/31	21.52	456	25.62

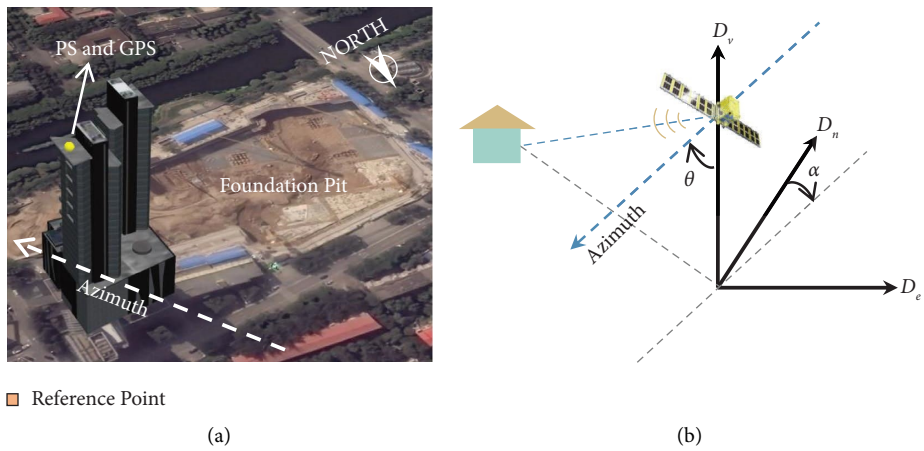

Figure 10: Satellite observation schematic of Kunlun Tower. (a) Site overview. (b) Satellite observation geometry.

was extracted. Subsequently, based on the geometric relationships illustrated in Figure 10(b), the authors in (12) was employed to combine the GPS-observed three-dimensional deformation components into the LOS deformation corresponding to the Sentinel-1 observation perspective. Ultimately, as shown in Figure 11, it can be observed that the observational results from GPS and PSI closely align in terms of trends, with measured deviations all within 5 mm. Deviations in the observational results may primarily stem from the inconsistent observation frequencies between the GPS monitoring station and the Sentinel satellite. Additionally, it should be noted that the discontinuity in the GPS deformation observation curve is caused by missing monitoring data. Therefore, it can be demonstrated that the combination of Sentinel-1 satellite imagery with PSI technology, coupled with the incorporation of ECMWF temperature data, enables an accurate observation of deformations in high-rise buildings.

$$D_{LOS} = \cos\theta D_v - \sin\theta \sin\alpha D_n + \sin\theta \cos\alpha D_e. \quad (12)$$

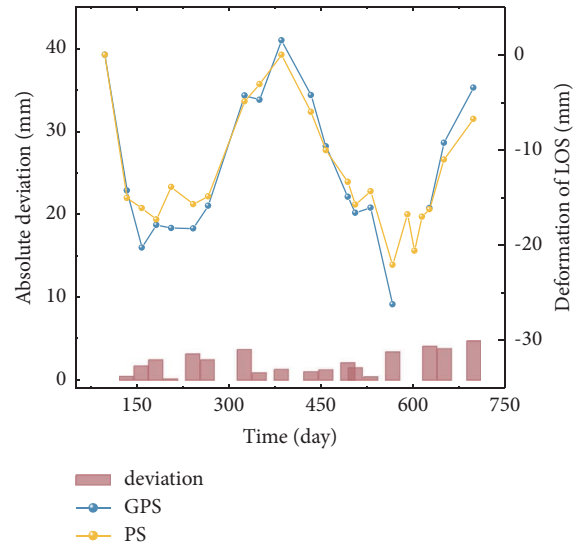

Figure 11: Comparison between PS results and GPS results.

4. Recognition of Building Deformation Patterns

4.1. Study Area. To validate the deformation identification and quantification method proposed in Sections 2.2, 2.3, and 2.4, this study conducted a practical analysis of a cluster of high-rise buildings in Changsha City, China. As the capital of Hunan Province, Changsha has undergone rapid development over the past 20 years resulting in a population of over 10 million and in dense clusters of high-rise buildings. It is therefore essential to employ an economical and efficient method to monitor the deformation status of the high-rise building clusters in Changsha, to reveal abnormal conditions such as building tilt. The study area is located within an 81 km^2 region centered at 28.22°N latitude and 113.00°E longitude. In this study, the Sentinel-1 images covering the period from November 2021 to September 2023, comprising a total of 53 images, were utilized for the high-rise building deformation analysis. The master image was acquired on December 6, 2022, and all images were ascending data with an incidence angle θ of 33.98° and an azimuth angle α of 169.18°. The temperature data, sourced from ECMWF, represents the average temperature in the study area at the corresponding moment of SAR imagery. More detailed imaging information is presented in Table 2.

As depicted in Figure 12, a bright pixel was selected as the Ground Control Point (GCP) in the mean amplitude image during this study. Subsequently, the mean amplitude image was projected onto the optical satellite map based on the latitude and longitude coordinates of the GCP. The image clearly delineates the outlines of numerous high-rise buildings along both banks of the Xiangjiang River, attributable to the strong backscatter properties of the facades of these structures. Subsequently, Figure 13 illustrates some of the PSs identified within the study area based on the PSI technique process described in Section 2.1. The circular markers in Figure 13 denote the positions of the identified PS, with colors representing a rough estimate of the LOS deformation rates.

Table 2: Changsha SAR image dataset.

No.	Slave	B (m)	t (day)	T (°C)
1	2021/11/05	−72.66	−396	18.56
2	2021/11/17	−32.55	−384	14.03
3	2021/11/29	−0.89	−372	15.71
4	2021/12/11	39.98	−360	11.25
5	2021/12/23	−50.60	−348	14.05
6	2022/01/04	−53.96	−336	9.82
7	2022/01/16	−58.78	−324	7.71
8	2022/01/28	−65.60	−312	2.32
9	2022/02/09	3.91	−300	4.20
10	2022/02/21	66.04	−288	4.09
11	2022/03/05	−1.24	−276	15.00
12	2022/03/17	−63.83	−264	11.57
13	2022/03/29	−2.482	−252	18.04
14	2022/04/10	−19.14	−240	26.61
15	2022/04/22	51.89	−228	21.57
16	2022/05/04	−153.5	−216	23.39
17	2022/05/16	8.11	−204	19.64
18	2022/05/28	7.93	−192	22.48
19	2022/06/09	118.00	−180	28.04
20	2022/06/21	47.84	−168	27.70
21	2022/07/03	15.24	−156	27.42
22	2022/07/15	−26.71	−144	33.80
23	2022/07/27	−29.65	−132	32.17
24	2022/08/08	98.31	−120	34.48
25	2022/09/13	95.11	−84	30.55
26	2022/09/25	−169.5	−72	25.19
27	2022/10/07	−76.10	−60	12.90
28	2022/11/12	−44.47	−24	18.46
29	2022/11/24	108.50	−12	16.81
30	2022/12/18	−54.08	12	5.96
31	2022/12/30	27.09	24	7.63
32	2023/01/11	−162.30	36	14.38
33	2023/01/23	40.00	48	7.07
34	2023/02/04	−22.09	60	5.38
35	2023/02/16	−146.90	72	10.02
36	2023/02/28	66.79	84	14.53
37	2023/03/12	5.58	96	16.25
38	2023/03/24	−2.68	108	11.22
39	2023/04/05	−78.82	120	12.48
40	2023/04/17	−1.77	132	30.19
41	2023/04/29	100.60	144	19.16
42	2023/05/11	15.31	156	18.66
43	2023/05/23	−22.56	168	17.85
44	2023/06/04	−13.25	180	27.60
45	2023/06/16	19.79	192	27.10
46	2023/06/28	−157.60	204	32.30
47	2023/07/10	125.90	216	34.14
48	2023/07/22	40.83	228	29.87
49	2023/08/15	−54.88	252	30.29
50	2023/08/27	110.30	264	22.62
51	2023/09/08	126.70	276	30.33
52	2023/09/20	56.45	288	23.55

To compare and verify the deformation recognition results and study the evolution patterns of building deformations, nine typical high-rise buildings with different construction times were chosen for analysis. Detailed information about the building can be found in Table 3, and the detected PSs on these building facades can be found in Figure 13. Because α_i is solely related to the relative positions among PSs, the calculation procedure directly employed the height values of PSs before the subtraction of DEM heights, thereby reducing the precision requirements for the DEM.

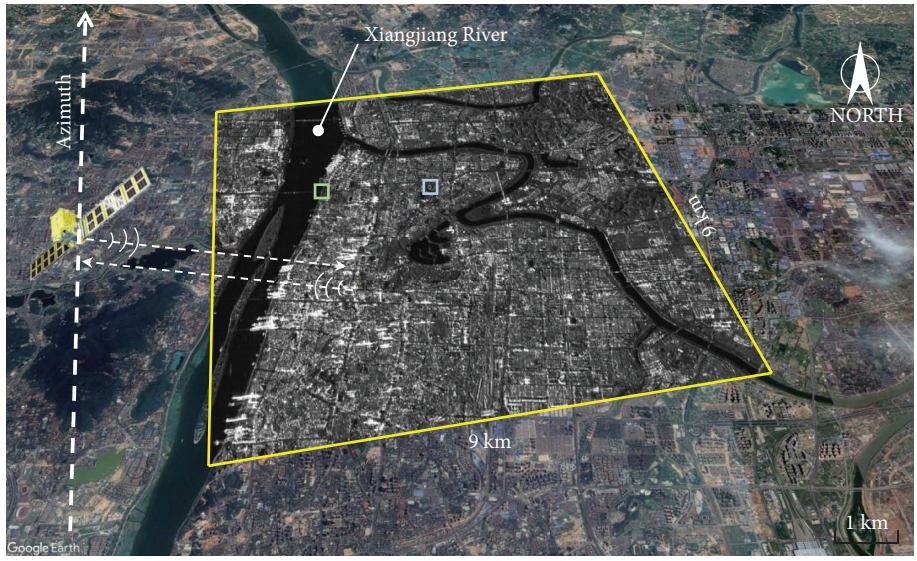

FIGURE 12: Average amplitude images displayed on Google Earth.

4.2. Buildings Deformed with Pattern I. Figures 14, 15, and 16 present the deformation recognition results for the International Finance Tower, Wanda Tower, and Huijing Tower. In all subfigures labeled (a), the timeline begins with the acquisition time of the first SAR image (November 5, 2021), where the height axis corresponds to the height values of PSs represented by different colors, and the vertical axis indicates the LOS deformation values for these PSs at various heights on the building facades. The LOS deformation of all PSs exhibits the seasonal temperature-induced deformation characteristic, with deformation amplitudes positively correlated to their respective heights. Evidently, the actual deformation curves of PSs are intricate, resulting in the challenge of determining the building deformation pattern through the calculation of A_i values described in Section 2.2. Therefore, it is necessary to utilize (7) to calculate the temperature-related deformation coefficient (α_i) and subsequently identify the deformation patterns of the buildings. In Figures 14(b), 15(b), and 16(b), the computed results of parameter α_i for high-rise buildings are presented along with the absolute deviation of α_i calculated using (10). It is observed that the absolute deviation values of α_i ($|\Delta\alpha|$) for these buildings are generally less than 1×10^{-6}/°C, consistent with the defined in Section 2.4 for deformation Pattern I. It should be emphasized that some significant outliers in the absolute deviation of α_i for the three buildings at certain identical moments, possibly arising from inaccuracies in temperature input, have been excluded from the analysis.

Due to the stable α_i identified from these three buildings, it can be inferred that only temperature-induced deformations are present. In this case, the concept of α_i can be comparable to the thermal expansion coefficient of reinforced steel or concrete materials. Significantly, the mean values of α_i for the three buildings are 6.66×10^{-6}/°C, 6.36×10^{-6}/°C, and 9.36×10^{-6}/°C, respectively, all located in the interval of the coefficient of the thermal expansion of reinforced steel or concrete material of $6\sim12\times10^{-6}$/°C.

4.3. Buildings Deformed with Pattern II. Huayaun Tower, Hilton Hotel, and Jinyu Tower exhibit similar trends in the evolution of the coefficient α_i. Figures 17, 18, and 19 present the deformation recognition results for these buildings. The three corresponding subplots labeled as (a) present the observed deformation results of PSs on the facades of these three high-rise buildings, revealing significantly distinct temperature-related deformation characteristics for each building. In all subplots (b), the coefficient α_i has been segmented into four sections, and the segmentation points correspond to the zero points of the deformation curves in plot (a). Furthermore, the value of α_i demonstrates a consistent increase during the cooling period and a sustained decrease during the warming period, aligning with the analysis of Pattern II in Section 2.4.

For the Huayuan Tower, a linear fit to the values of α_i reveals a change rate $k=1.19\times10^{-9}$/°C·d. Furthermore, using (11), the cumulative LOS deformation at the top of the building can be calculated over the observation period of 672 days (time span covered from the second image to the last image), resulting in $D_{LOS}^{top}=0.93$mm. Given the small magnitude of this displacement, assuming it is entirely attributed to the reduction in building height (shrinkage or creep), the vertical displacement of the structure can be calculated as 1.12 mm using (12). For the Hilton Hotel, the calculated change rate for α_i is $k=1.36\times10^{-9}$/°C•d. Similarly, the vertical displacement at the top of can be calculated

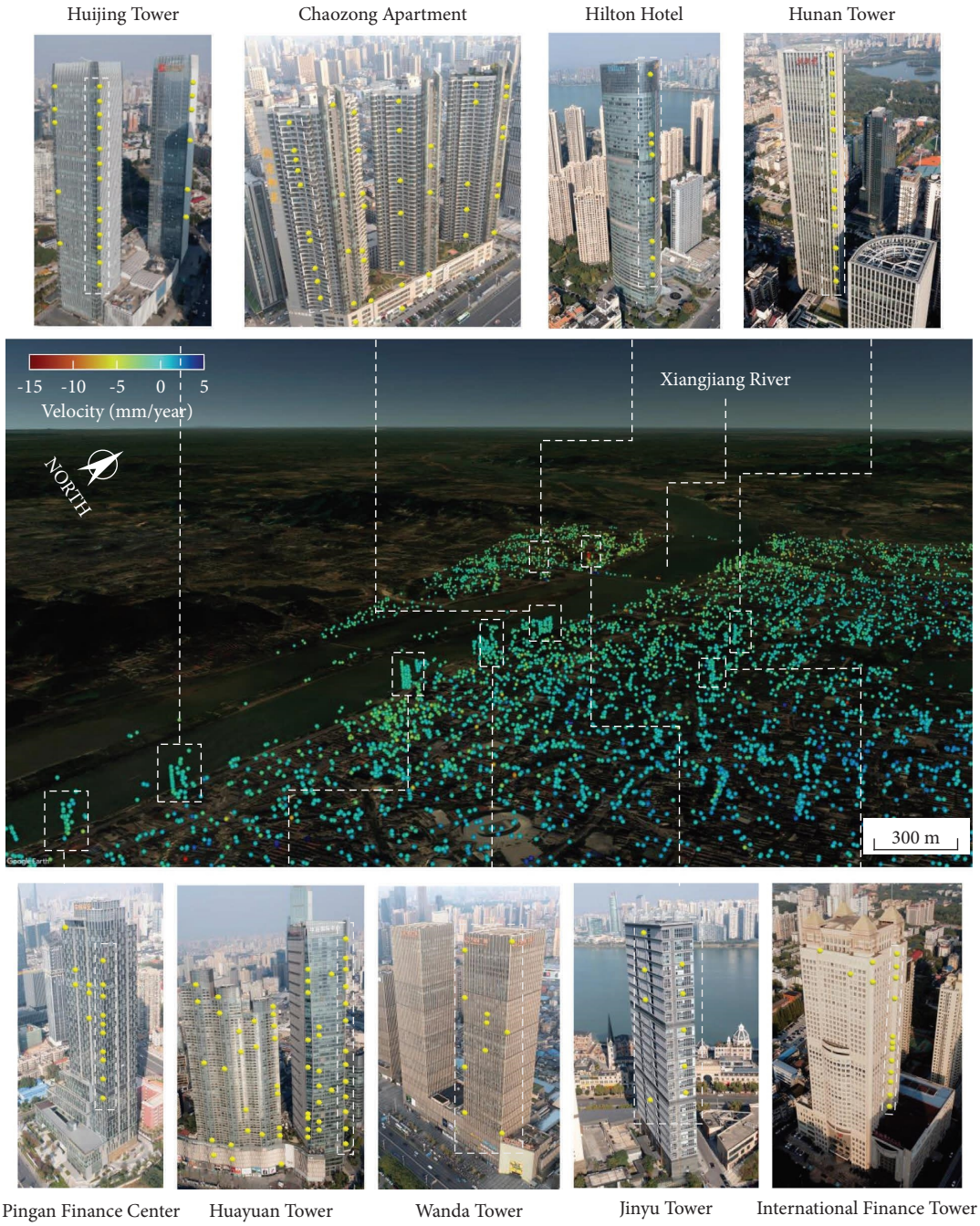

Figure 13: Distribution of PSs (dashed box lines indicate the selected PSs used for calculations).

Table 3: Statistical information on typical high-rise buildings.

Building	H (m)	Year
International Finance Tower	182	2001
Wanda Tower	200	2012
Huijing Tower	230	2018
Huayuan Tower	258	2015
Hilton Hotel	241	2017
Jinyu Tower	150	2021
Chaozong Apartment	117	2012
Hunan Tower	248	2015
Pingan Finance Center	211	2020

as 1.20 mm over the 672 days. Additionally, the Jinyu Tower exhibited a distinct Pattern II deformation, with a change rate of α_i denoted as $k = 3.26 \times 10^{-8}$/°C·d. Furthermore, over the same study period, the LOS deformation at the top of the building can be calculated as $D_{LOS}^{top} = 14.89$mm, equivalent to a vertical deformation of 17.96 mm. It is noteworthy that the construction completion time of the Jinyu Tower is very close to the starting point of the study period. A larger deformation implies that the building was undergoing more significant shrinkage and creep. However, from a civil engineering perspective, this relatively larger deformation

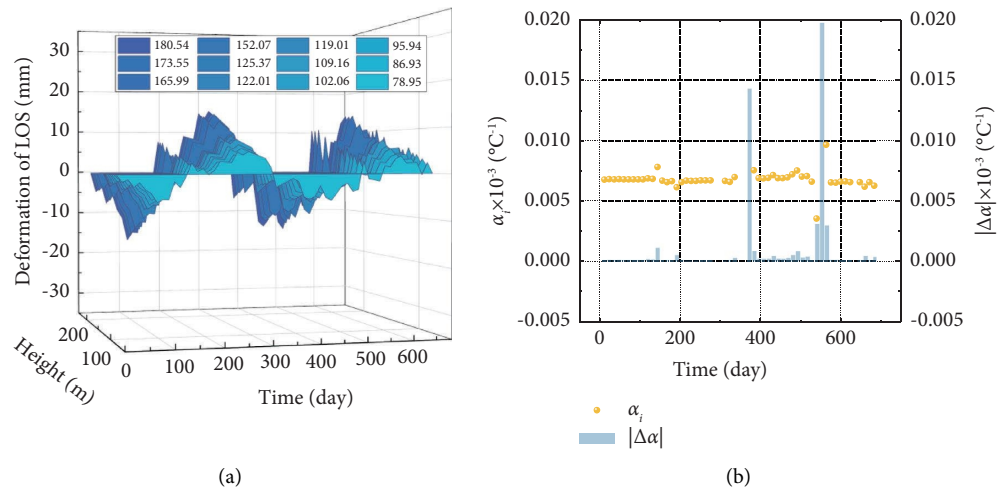

FIGURE 14: The deformation recognition result of International Finance Tower. (a) Deformation results of the PSs. (b) Evolution of α_i and absolute deviation.

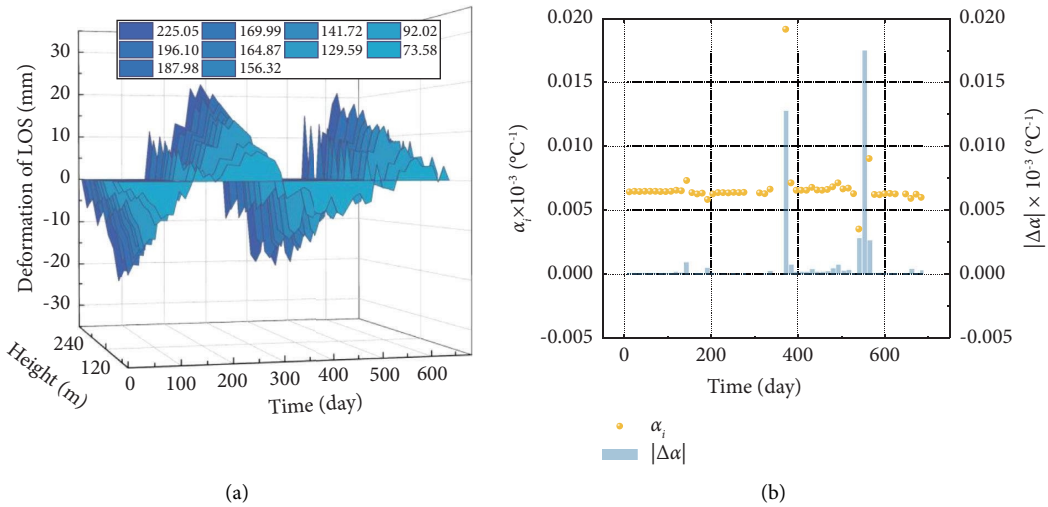

FIGURE 15: Deformation recognition result of Wanda Tower. (a) Deformation results of the PSs. (b) Evolution of α_i and absolute deviation.

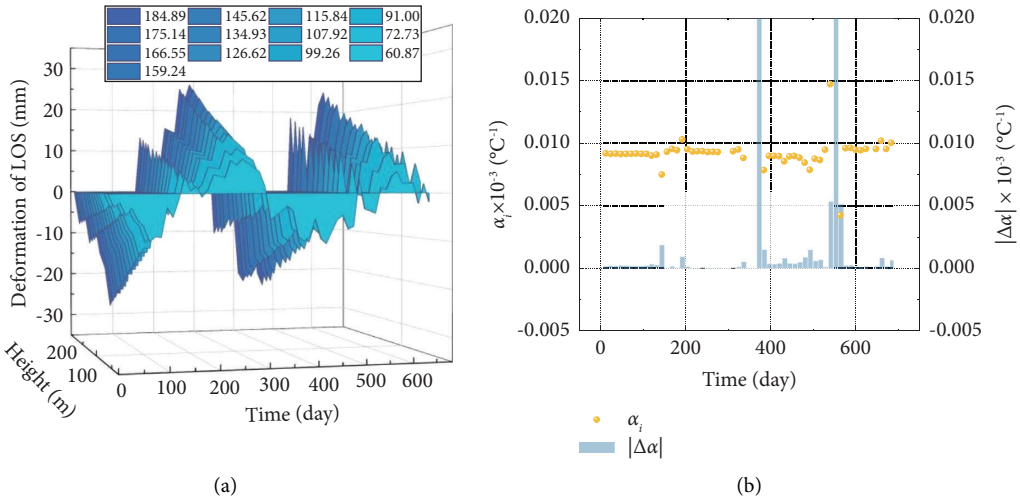

FIGURE 16: Deformation recognition result of Huijing Tower. (a) Deformation results of the PSs. (b) Evolution of α_i and absolute deviation.

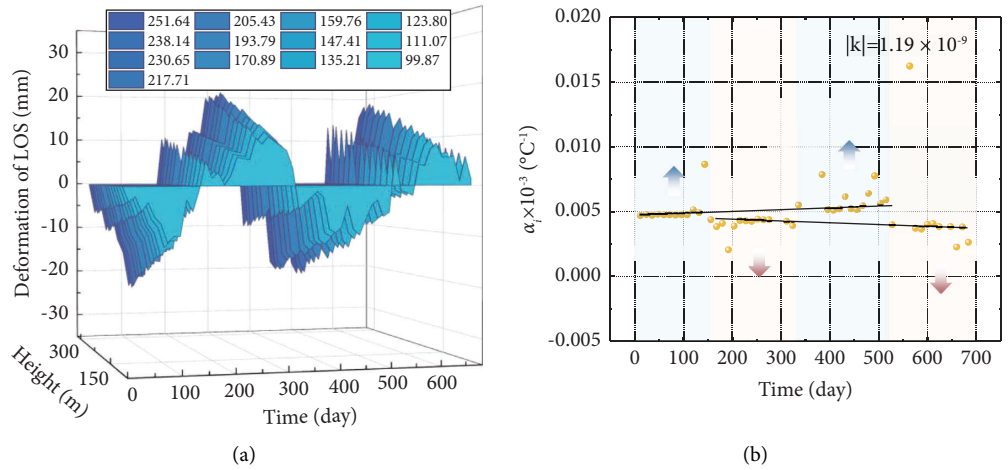

FIGURE 17: Deformation recognition result of Huayuan Tower. (a) Deformation results of the PSs. (b) Evolution of α_i and absolute deviation.

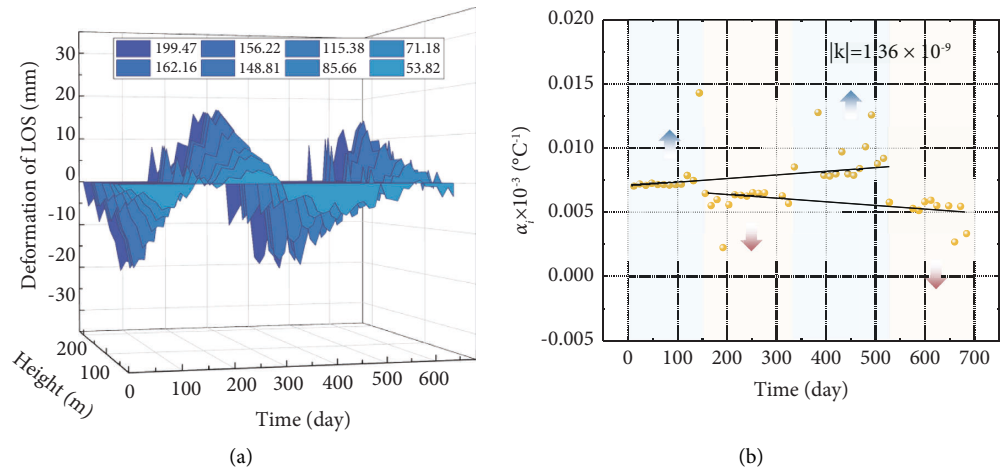

FIGURE 18: Deformation recognition result of Hilton Tower. (a) Deformation results of the PSs. (b) Evolution of α_i and absolute deviation.

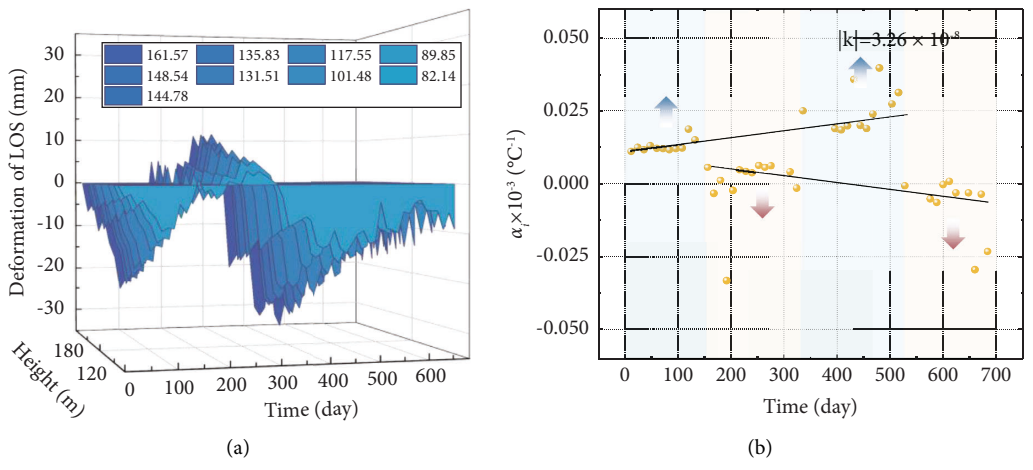

FIGURE 19: Deformation recognition result of Jinyu Tower. (a) Deformation results of the PSs. (b) Evolution of α_i and absolute deviation.

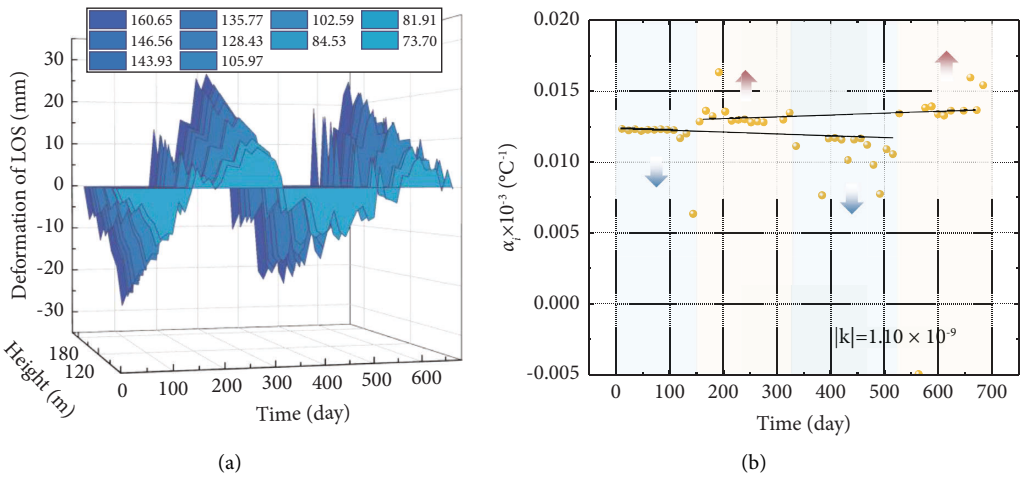

FIGURE 20: Deformation recognition result of Chaozong apartment, (a) Deformation results of the PSs. (b) Linear fitting result for α_i.

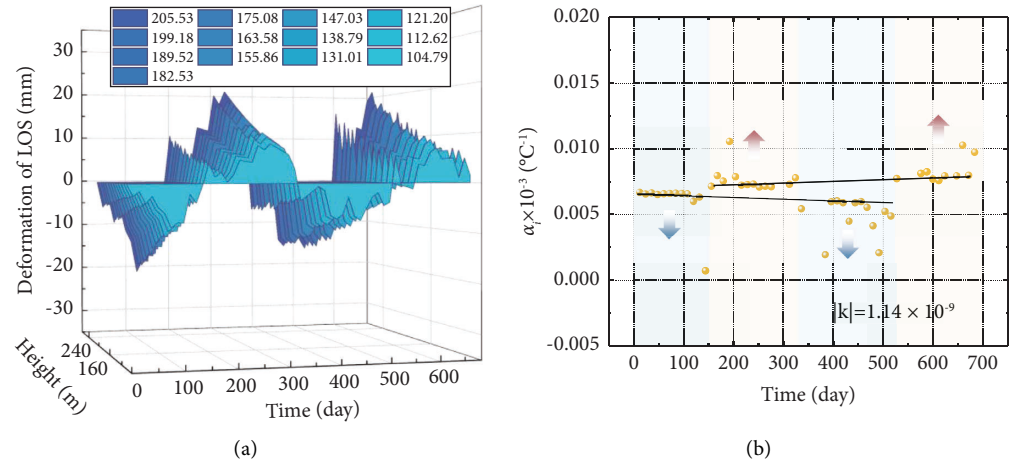

FIGURE 21: Deformation recognition result of Hunan Tower. (a) Deformation results of the PSs. (b) Linear fitting result for α_i.

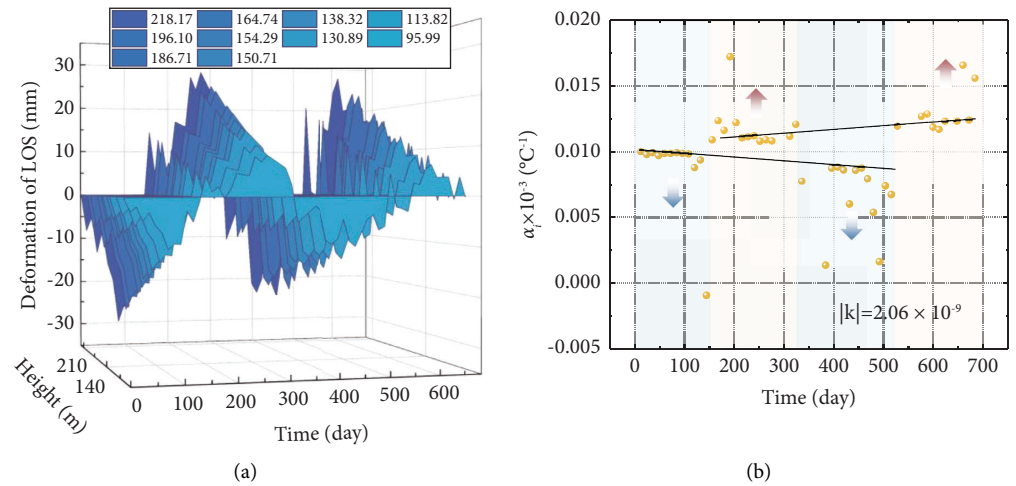

FIGURE 22: Deformation recognition result of Pingan Finance Center. (a) Deformation results of the PSs. (b) Linear fitting result for α_i.

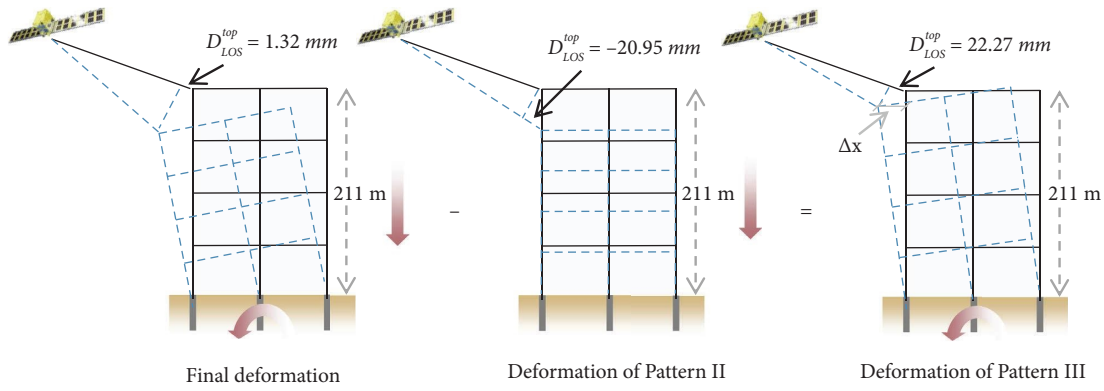

Figure 23: Possible mixed deformation patterns for Pingan Finance Center.

Table 4: Results of deformation recognition.

Pattern	Building	$\alpha \times 10^{-6}$ (°C^{-1})	$k \times 10^{-9}$ (°C^{-1}·d^{-1})	Deformation	Quantification
I	International Finance Tower	6.66	—	—	—
	Wanda Tower	6.36	—	—	—
	Huijing Tower	9.36	—	Inclination + shrinkage/creep	—
II	Huayuan Tower	4.68	1.19	Shrinkage/creep	4.34×10^{-6}
	Hilton Hotel	7.02	1.36	Shrinkage/creep	4.98×10^{-6}
	Jinyu Tower	11.09	32.6	Shrinkage/creep	1.20×10^{-4}
III	Chaozong Apartment	12.33	1.10	Inclination	5.98×10^{-6}
	Hunan Tower	6.67	1.14	Inclination	6.21×10^{-6}
	Pingan Finance Center	10.00	2.06	Inclination + shrinkage/creep	1.89×10^{-4}

value still falls within the reasonable range for shrinkage and creep in newly constructed reinforced concrete structures.

4.4. Buildings with Pattern III. The results of the deformation recognition for Chaozong Apartment, Hunan Tower, and Pingan Finance Center are presented in Figures 20, 21, 22. All subfigures (a) display the deformation results of PSs on the facades of these three buildings. All subfigures (b) illustrate an evolution trend of α_i opposite to that discussed in Section 4.3, implying that the buildings have undergone Pattern III deformation.

Furthermore, this study similarly conducted a quantitative analysis of the deformations of these three buildings. For Chaozong Apartment, the rate of change of α_i can be determined as $k = 1.10 \times 10^{-9}$/°C·d, resulting in $D_{LOS}^{top} = 0.39$mm. Since pattern III deformation is caused by the building's inclination, the value of D_{LOS}^{top} can be converted into a horizontal displacement towards the satellite of 0.70 mm using (12). For Hunan Tower, the calculated change rate for α_i is $k = 1.14 \times 10^{-9}$/°C•d, resulting in a horizontal displacement towards the satellite of 1.54 mm at the top of the building.

It is noteworthy that the construction time of Pingan Finance Center is close to that of Jinyu Tower. In a general analysis, it is expected that Pingan Finance Center would undergo significant shrinkage and creep deformation during the observation period, exhibiting the characteristics of Pattern II. However, as shown in Figure 22(b), the evolution of α_i exhibits a typical characteristic of Pattern III deformation. The change rate for α_i is calculated to be $k = 2.06 \times 10^{-9}$/°C·d, resulting in a final deformation of $D_{LOS}^{top} = 1.32$ mm. To analyze the anomalous deformation pattern of Pingan Finance Center further, it is assumed that it has experienced the same degree of Pattern II deformation as the Jinyu Building. Therefore, Ping An Finance Center may have undergone a LOS deformation of 17.96 mm/150000 mm × 211000 mm × cos33.98° = 20.95 mm towards the satellite, masking the shrinkage and creep deformation of the building away from the satellite in the LOS direction. Through the analysis depicted in Figure 23, it is determined that the LOS deformation induced by tilting at the top of Pingan Finance Center is 22.27 mm, corresponding to a horizontal displacement of $\Delta x = 39.85$ mm. Such deformation could be attributed to the initial uneven shrinkage and creep in the early stages of construction.

4.5. Comparative Analysis. Table 4 summarizes the results of the analysis of the buildings. Regarding the statistical analysis of α for buildings under Pattern I, the average values of α_i were used, while the initial values of α_i were employed for the other two patterns. This stipulation ensures that α has maximum comparability with the thermal expansion coefficient of the material. In terms of deformation quantification, to ensure comparability of quantified values across different buildings, the ratio of building top displacement to the corresponding building height was computed.

From the statistical analysis of α, it can be observed that nearly all the values are within the range of $6\sim12\times10^{-6}/°C$, which is consistent with the coefficient of thermal expansion of reinforced steel or concrete materials, except for the Huayuan Tower and Chaozong Apartment. The different values of α may be associated with varying structural forms or building materials. From the perspective of building deformation, International Finance Tower and Wanda Tower, both with a service life exceeding 10 years, maintain stability in terms of shrinkage and creep deformation. The Huijing Tower, which was completed in 2018, exhibited stable deformation characteristics, possibly due to undergoing complex deformations similar to those observed in the Pingan Finance Center. Furthermore, examining the three buildings in Pattern II, it is observed that the earlier the construction completion, the milder shrinkage and creep, providing further confirmation of the validity of the calculated deformation results in this study. Additionally, according to the Chinese Code for Design of Building Foundation (GB50007-2011) [45], the ratio of lateral displacement to build height for high-rise buildings over 100 meters should not exceed 0.002. This ratio for the three buildings in Pattern III is 5.98×10^{-6}, 6.20×10^{-6}, and 1.89×10^{-4}, respectively, all of which are below the threshold of 0.002.

5. Conclusions

This study combined Sentinel-1 image data with PSI technology to observe the deformation of high-rise buildings in Changsha City from November 2021 to September 2023. The main research findings and conclusions are summarized as follows:

(1) This study validated ECMWF temperature data using temperature recordings from transducers on a high-rise building. The results indicate that the expected value of the normal distribution of ECMWF temperature deviation approaches zero, making it applicable to the deformation solution in the PSI technique for high-rise buildings. Additionally, the accuracy of combining Sentinel-1 image data with PSI technology for high-rise building deformation analysis was verified to be superior to 5 mm through GPS deformation monitoring data on the Beijing Kunlun Tower.

(2) From the unique observational perspective of SAR satellites, this study systematically analyzed the deformation patterns of high-rise buildings and summarized three typical deformation patterns. Furthermore, the concept and algorithm of temperature-related deformation coefficients were proposed, along with a method to quantify building deformation based on the rate of change of temperature-related deformation coefficients. Finally, the research findings indicate that the proposed method effectively mitigates the interference of temperature-induced deformations in the identification process of anomalous building deformations, enabling analysis of complex deformations in high-rise buildings at a millimeter-scale level.

(3) Through deformation analysis of nine high-rise buildings in Changsha, it was observed that the thermal expansion coefficients of the majority of buildings fall within the range of $6\sim12\times10^{-6}/°C$, which is similar to the thermal expansion coefficients of building materials. Furthermore, the study reveals that the deformations of buildings older than ten years are highly stable, whereas newly constructed buildings may experience a contraction creep of up to 1.20×10^{-4} mm/mm within two years. Notably, super-tall buildings may exhibit centimeter-scale lateral deformations at their tops due to uneven shrinkage.

However, there are still areas for further improvement in this study. For instance, integrating multiangle SAR images to obtain more comprehensive building deformation information, utilizing higher-precision temperature data to improve the accuracy of building deformation analysis, and combining the algorithm with internal force and stress analysis in structural engineering, such as finite element methods would all contribute to enhancing the reliability of building deformation monitoring.

Data Availability

The data used to support the findings of this study are available from the corresponding author upon reasonable request.

Conflicts of Interest

The authors declare that there are no conflicts of interest regarding the publication of this paper.

Acknowledgments

The authors sincerely appreciate the funding support provided by the National Natural Science Foundation of China (NSFC) (No. 52278306), the Key Research and Development Program of Hunan Province (No. 2022SK2096), the Hunan Provincial Natural Science Foundation of China (No. 2023JJ70003), the Science and Technology Progress and Innovation Project of Department of Transportation of Hunan Province (No. 201912), and the Hydraulic Science and Technology Project of the Hunan Provincial Department of Water Resources (XSKJ2023059-31). The authors also sincerely thank Professor Yan Bao from the Beijing University of Technology and Professor Guoquan Wang from the University of Houston for providing accurate GPS monitoring data for Kunlun Tower.

References

[1] B. B. Hanberry, "Urban land expansion and decreased urban sprawl at global, national, and city scales during 2000 to 2020," *Ecosystem Health and Sustainability*, vol. 9, 2023.

[2] S. Y. Lin, "Urban hazards caused by ground deformation and building subsidence over fossil lake beds: a study from Taipei City," *Geomatics, Natural Hazards and Risk*, vol. 13, no. 1, pp. 2890–2910, 2022.
[3] Y. Bao, W. Guo, G. Q. Wang, W. J. Gan, M. J. Zhang, and J. S. Shen, "Millimeter-accuracy structural deformation monitoring using stand-alone GPS: case study in Beijing, China," *Journal of Surveying Engineering*, vol. 144, no. 1, 2018.
[4] Y. Z. Liu, W. X. Cao, Z. Q. Shi et al., "Evaluation of post-tunneling aging buildings using the InSAR nonuniform settlement index," *Remote Sensing*, vol. 15, no. 14, p. 3467, 2023.
[5] J. P. Stewart, N. Wagner, D. Murphy et al., "Foundation settlement and tilt of millennium tower in San Francisco, California," *Journal of Geotechnical and Geoenvironmental Engineering*, vol. 149, no. 6, 2023.
[6] R. W. Parkinson, "Speculation on the role of sea-level rise in the tragic collapse of the Surfside condominium Miami Beach, Florida USAwas a bellwether moment for coastal zone management practitioners," *Ocean and Coastal Management*, vol. 215, Article ID 105968, 2021.
[7] L. B. Pan, P. C. Liu, and S. L. Bakoss, "Long-term shortening of concrete columns in tall buildings," *Journal of Structural Engineering*, vol. 119, no. 7, pp. 2258–2262, 1993.
[8] P. F. Ma, H. Lin, H. X. Lan, and F. L. Chen, "Multi-dimensional SAR tomography for monitoring the deformation of newly built concrete buildings," *ISPRS Journal of Photogrammetry and Remote Sensing*, vol. 106, pp. 118–128, 2015.
[9] T. Lovas, A. Barsi, A. Detrekoi et al., "Terrestrial laser scanning in deformation measurements of structures," *The International Archives of the Photogrammetry, Remote Sensing and Spatial Information Sciences*, vol. 37, no. B5, pp. 527–532, 2008.
[10] N. Cavalagli, A. Kita, S. Falco, F. Trillo, M. Costantini, and F. Ubertini, "Satellite radar interferometry and in-situ measurements for static monitoring of historical monuments: the case of Gubbio, Italy," *Remote Sensing of Environment*, vol. 235, Article ID 111453, 2019.
[11] T. Kijewski-Correa, D. K. Kwon, A. Kareem et al., "Smartsync: an integrated real-time structural health monitoring and structural identification system for tall buildings," *Journal of Structural Engineering*, vol. 139, no. 10, pp. 1675–1687, 2013.
[12] R. M. Mateos, J. M. Azañón, F. J. Roldán et al., "The combined use of PSInSAR and UAV photogrammetry techniques for the analysis of the kinematics of a coastal landslide affecting an urban area (SE Spain)," *Landslides*, vol. 14, no. 2, pp. 743–754, 2017.
[13] X. Z. Yu, Y. Q. Ge, T. L. Zhao, G. J. Zhang, Y. C. Liu, and C. X. Yu, "The dynamic displacement monitoring method using unmanned aerial vehicles based on digital close-range photogrammetry," *Mathematical Problems in Engineering*, vol. 2022, pp. 1–10, Article ID 1949213, 2022.
[14] T. Lipecki, "Non-contact diagnostics of the geometry of a historic wooden building as an element of periodic safety assessment," *Sensors*, vol. 22, no. 4, p. 1301, 2022.
[15] M. Guo, M. X. Sun, D. Pan et al., "High-precision detection method for large and complex steel structures based on global registration algorithm and automatic point cloud generation," *Measurement*, vol. 172, Article ID 108765, 2021.
[16] M. Crosetto, O. Monserrat, M. Cuevas-González, N. Devanthéry, G. Luzi, and B. Crippa, "Measuring thermal expansion using X-band persistent scatterer interferometry," *ISPRS Journal of Photogrammetry and Remote Sensing*, vol. 100, pp. 84–91, 2015.
[17] G. J. Zhang, Z. Wang, W. Sang et al., "Research on dynamic deformation laws of super high-rise buildings and visualization based on GB-RAR and LiDAR technology," *Remote Sensing*, vol. 15, no. 14, p. 3651, 2023.
[18] A. K. Gabriel, R. M. Goldstein, and H. A. Zebker, "Mapping small elevation changes over large areas: differential radar interferometry," *Journal of Geophysical Research: Solid Earth*, vol. 94, no. B7, pp. 9183–9191, 1989.
[19] P. F. Ma, H. Lin, W. X. Wang et al., "Toward Fine Surveillance: a review of multitemporal interferometric synthetic aperture radar for infrastructure health monitoring," *IEEE Geoscience and Remote Sensing Magazine*, vol. 10, no. 1, pp. 207–230, 2022.
[20] A. Ferretti, C. Prati, and F. Rocca, "Permanent scatterers in SAR interferometry," *IEEE Transactions on Geoscience and Remote Sensing*, vol. 39, no. 1, pp. 8–20, 2001.
[21] A. Ferretti, C. Prati, and F. Rocca, "Nonlinear subsidence rate estimation using permanent scatterers in differential SAR interferometry," *IEEE Transactions on Geoscience and Remote Sensing*, vol. 38, no. 5, pp. 2202–2212, 2000.
[22] M. Crosetto, O. Monserrat, R. Iglesias, and B. Crippa, "Persistent scatterer interferometry: potential, limits and initial C- and X-band comparison," *Photogrammetric Engineering and Remote Sensing*, vol. 76, no. 9, pp. 1061–1069, 2010.
[23] A. Ferretti, G. Savio, R. Barzaghi et al., "Submillimeter accuracy of insar time series: experimental validation," *IEEE Transactions on Geoscience and Remote Sensing*, vol. 45, no. 5, pp. 1142–1153, 2007.
[24] K. Karila, M. Karjalainen, J. Hyyppä, J. Koskinen, V. Saaranen, and P. Rouhiainen, "A comparison of precise leveling and persistent scatterer SAR interferometry for building subsidence rate measurement," *ISPRS International Journal of Geo-Information*, vol. 2, no. 3, pp. 797–816, 2013.
[25] K. Yang, L. Yan, G. M. Huang, C. Chen, and Z. P. Wu, "Monitoring Building deformation with insar:experiments and validation," *Sensors*, vol. 16, no. 12, p. 2182, 2016.
[26] A. Ciampalini, F. Bardi, S. Bianchini et al., "Analysis of building deformation in landslide area using multisensor PSInSAR™ technique," *International Journal of Applied Earth Observation and Geoinformation*, vol. 33, pp. 166–180, 2014.
[27] B. Osmanoglu, T. H. Dixon, S. Wdowinski, E. Cabralcano, and Y. Jiang, "Mexico City subsidence observed with persistent scatterer InSAR," *International Journal of Applied Earth Observation and Geoinformation*, vol. 13, no. 1, pp. 1–12, 2011.
[28] D. Perissin and T. Wang, "Time-Series InSAR applications over urban areas in China," *Ieee Journal of Selected Topics in Applied Earth Observations and Remote Sensing*, vol. 4, no. 1, pp. 92–100, 2011.
[29] S. Bianchini, F. Pratesi, T. Nolesini, and N. Casagli, "Building deformation assessment by means of persistent scatterer interferometry analysis on a landslide-affected area: the Volterra Italycase study," *Remote Sensing*, vol. 7, no. 4, pp. 4678–4701, 2015.
[30] A. Drougkas, E. Verstrynge, K. Van Balen et al., "Country-scale InSAR monitoring for settlement and uplift damage calculation in architectural heritage structures," *Structural Health Monitoring*, vol. 20, no. 5, pp. 2317–2336, 2021.
[31] V. Macchiarulo, P. Milillo, M. J. Dejong, J. González Martí, J. Sánchez, and G. Giardina, "Integrated InSAR monitoring and structural assessment of tunnelling-induced building deformations," *Structural Control and Health Monitoring*, vol. 28, no. 9, p. e2781, 2021.

[32] W. Q. Wu, H. T. Cui, J. Hu, and L. Yao, "Detection and 3D visualization of deformations for high-rise buildings in Shenzhen, China from high-resolution TerraSAR-X Datasets," *Applied Sciences*, vol. 9, no. 18, p. 3818, 2019.

[33] M. Zhu, X. Wan, B. G. Fei et al., "Detection of building and infrastructure instabilities by automatic spatiotemporal analysis of satellite sar interferometry measurements," *Remote Sensing*, vol. 10, no. 11, p. 1816, 2018.

[34] S. Gernhardt and R. Bamler, "Structural deformation and non-seasonal motion of single buildings in urban areas revealed by PSI," in *Proceedings of the IEEE Conference: Joint Urban Remote Sensing Event*, *2015 Joint Urban Remote Sensing Event (JURSE)*, Lausanne, Switzerland, May 2015.

[35] H. S. Jung, Z. Lu, and L. Zhang, "Feasibility of along-track displacement measurement from sentinel-1 interferometric wide-swath mode," *IEEE Transactions on Geoscience and Remote Sensing*, vol. 51, no. 1, pp. 573–578, 2013.

[36] M. Besoya, H. Govil, and P. Bhaumik, "A review on surface deformation evaluation using multitemporal SAR interferometry techniques," *Spatial Information Research*, vol. 29, no. 3, pp. 267–280, 2021.

[37] N. Adam, A. Parizzi, M. Eineder, and M. Crosetto, "Practical persistent scatterer processing validation in the course of the Terrafirma project," *Journal of Applied Geophysics*, vol. 69, no. 1, pp. 59–65, 2009.

[38] S. Gernhardt, N. Adam, M. Eineder, and R. Bamler, "Potential of very high resolution sar for persistent scatterer interferometry in urban areas," *Annals of GIS*, vol. 16, no. 2, pp. 103–111, 2010.

[39] R. A. Ramirez, G. J. Lee, S. K. Choi et al., "Monitoring of construction-induced urban ground deformations using Sentinel-1 PS-InSAR: the case study of tunneling in Dangjin, Korea," *International Journal of Applied Earth Observation and Geoinformation*, vol. 108, Article ID 102721, 2022.

[40] R. A. Ramirez, R. E. E. Abdullah, and C. J. P. Rubio, "S1-PSInSAR Monitoring and hyperbolic modeling of nonlinear ground subsidence in Naga City, Cebu Island in the Philippines," *International Journal of GEOMATE*, vol. 23, no. 100, pp. 102–109, 2022.

[41] A. Ferretti, A. Monti-Guarnieri, C. Prati, F. Rocca, and D. Massonnet, "InSAR principles-guidelines for SAR interferometry processing and interpretation," 2007, https://www.researchgate.net/publication/234226330.

[42] O. Monserrat, M. Crosetto, M. Cuevas, and B. Crippa, "The Thermal expansion component of persistent scatterer interferometry observations," *IEEE Geoscience and Remote Sensing Letters*, vol. 8, no. 5, pp. 864–868, 2011.

[43] C. B. Haselton, A. B. Liel, G. G. Deierlein, B. S. Dean, and J. H. Chou, "Seismic collapse safety of reinforced concrete buildings. I: assessment of Ductile Moment Frames," *Journal of Structural Engineering*, vol. 137, no. 4, pp. 481–491, 2011.

[44] Y. Zhou, X. M. Luo, P. Ye, W. J. Zhang, L. H. Qin, and Z. Du, "Bayesian-based prediction and real-time updating of axial deformation in high-rise buildings during construction," *Engineering Structures*, vol. 297, Article ID 116992, 2023.

[45] China Architecture and Building Press, *GB5007-2011. Code for Design of Building Foundation*, China Architecture and Building Press, Beijing, China, 2011.